



Transonic accretion flow in the mini discs of a binary black hole system

Subhankar Patra ^{*}, Bibhas Ranjan Majhi [†] and Santabrata Das [‡]

Department of Physics, Indian Institute of Technology Guwahati, Guwahati 781039, Assam, India

(Dated: December 24, 2024)

We study the general relativistic transonic accretion flow around the primary black hole, which forms the circumprimary disc (CPD), within a BBH system. The BBH spacetime is characterized by the mass ratio (q) and the separation distance (z_2) between the two black holes. We numerically solve the radial momentum and energy equations to obtain the accretion solutions. It is observed that the CPD can exhibit shock solutions, which exist for a wide range parameter space spanned by flow angular momentum (λ) and energy (E). We find that the shock parameter space is modified by q and z_2 . Investigations show that q and z_2 also affect various shock properties, such as density compression and temperature compression across the shock fronts. Moreover, we calculate the spectral energy distributions (SEDs) of the CPD and examine how the SEDs are modified by q and z_2 for both shock-free and shock-induced accretion solutions. SED is found to be nearly independent of the binary parameters. We depict that the mutual interaction between two black holes in a binary system hardly alters their individual accretion features. This study replicates the existing predictions in a different context of binary accretion.

Keywords: accretion; accretion discs; black hole physics; hydrodynamics; shock waves

I. INTRODUCTION

Binary black hole (BBH) systems are powerful multi-messenger astrophysical sources of gravitational waves (GWs) and electromagnetic (EM) waves. The formation scenarios of BBHs are not clearly understood yet. In this regard, various astrophysical channels have been proposed in the literature. Notable studies by [1] and [2] indicate that supermassive black hole binaries (SMBHBs) form as a result of galaxy mergers. On the other hand, stellar-mass BBHs are generated through dynamic encounters in the environments of dense star clusters [3, 4]. Recently, it has been demonstrated that the gaseous dynamical friction can form a BBH system in the active galactic nucleus (AGN) discs [5].

In addition to the understanding of the formation channels of BBHs, detecting them through observations is also a vital aspect in astrophysics. Meanwhile, LIGO and Virgo collaborations reveal that the gravitational interactions within BBHs can produce GWs [6], as predicted by general relativity, thereby providing direct evidence of stellar-mass BBHs through GWs. On the other hand, SMBHBs at sub-parsec separations are the strong GW sources [7], which may be detectable by the Pulsar Timing Arrays [8] or the future mission Laser Interferometer Space Antenna [9, 10]. Like AGNs, BBHs can radiate across the electromagnetic spectrum due to the accretion of matter from the surroundings. Therefore, in addition to GWs, analyzing EM signature from BBHs is also crucial for their study. In recent years, several EM

observational works, including both the thermal and non-thermal emissions, have come out for the BBHs [11–20]. Indeed, these investigations provide the valuable information about the binary evolution, mass accretion rate, disc inclination angle, mass and the spin of the individual black holes, etc.

The accretion flow onto a BBH system is qualitatively different from a single black hole accretion. For BBH accretion, a truncated disc surrounds the entire binary system [21], called the circumbinary disc (CBD), where the matter flows inward due to the gravity of BBHs and the angular momentum transport through the viscous stress. Moreover, the tidal interaction between BBHs and CBD creates a cavity within the CBD, which defines its inner boundary. A significant fraction of the matter at this inner boundary falls toward the binary system and begins to orbit the individual black holes, resulting in the formation of a pair of mini discs. The mini discs surrounding the primary (more massive) and secondary (less massive) black holes are referred to as circumprimary discs (CPDs) and circumsecondary discs (CSDs), respectively. The presence of multiple discs (i.e., CBD, CPD, and CSD) complicates the study of BBH accretion compared to the accretion of individual black holes. Numerous theoretical models on BBHs accretion flow have been proposed in Newtonian gravity and general relativity (GR) [18, 19, 21–26, and references therein]. All these models based on different physical conditions and explained the dynamics of CBD, mini discs, role of magnetic field, outflows or jets and EM spectral signature, etc., which indeed help to distinguish them from the ordinary AGNs. However, to the best of our knowledge, no body has conveyed the transonic accretion flow for the BBH systems, where flow must satisfied the inner boundary condition set by the horizon [27, 28]. Toward this, for the first time we study the GR hydrodynamics of

* psubhankar@iitg.ac.in

† bibhas.majhi@iitg.ac.in

‡ sbdas@iitg.ac.in

transonic accretion flow in the background of a BBH metric [29], which represents a system of two Schwarzschild black holes in an external gravitational field. We expect this study may provide the better understanding of the BBHs.

Finding an exact analytical solution for binary or multiple black hole sources in GR is very challenging. Several attempts have been made to address this problem [30, 31], where it often requires the extra matter fields, commonly interpreted as struts or cosmological strings, to support the gravitational attraction between the black holes. However, all of them are hard to believe as a proper manifold because some fundamental theoretical issues arise regarding asymptotic flatness, singular behaviors, validity of energy conditions, etc., along with the stability issues. In [32–35], some regular metric solutions were proposed for the multi-black hole configurations. In these models, electromagnetic fields or charged matter help to maintain the equilibrium between the black holes. However, these systems are generally unstable to small perturbations, which could cause them to merge or drift apart. Astorino and Viganò [29] were the first to propose an exact analytical solution for a configuration of two static black holes, where an external back-reacting gravitational field maintains the equilibrium between two sources without requiring additional matter fields. Most importantly, this metric is regular everywhere outside the event horizons, i.e., free from any conical and curvature singularities, providing a physical BBH metric solution. It is characterized by the masses and positions of the two black holes, external field parameters, and a gauge parameter. In this work, we investigate the transonic accretion flow around the primary black hole in the background of this metric. We find both the shock-free and shock-induced accretion solutions, and examine their corresponding disc properties, such as density distribution, temperature distribution, and emissivity, etc. Since the horizon of individual Schwarzschild black holes are distorted by their mutual interactions, the presence of the secondary black hole may influence the accretion properties of the CPD. To address this possibility, we explore the impact of binary parameters, specifically the mass ratio (q) of the two black holes and their separation (z_2) on the accretion solutions. We also examine the various shock properties and luminosity distributions of the CPD as functions of q and z_2 . These investigations show that the accretion properties of the CPD are nearly independent of the binary parameters, featuring earlier predictions based on different aspects of binary accretion [19].

The paper is organized as follows. In Section II, we introduce the BBH spacetime. The model equations governing the accretion flow in the CPD are formulated in Section III. In Section IV, we present the transonic accretion solutions and discuss the impact of binary parameters on various accretion properties. Finally, we present the concluding remarks in Section V.

II. BINARY BLACK HOLE SPACETIME

Astrophysical black holes are always embedded in external gravitational fields, which can be described by a series of multipole moments. It has been shown in [36] that any non-spherical matter distributions, such as accretion discs, galaxies, nebulae, etc., will generally produce a multipolar gravitational field. These external gravitational fields provide a physical mechanism to maintain the equilibrium between the black holes. The line element of a system of two Schwarzschild black holes immersed in a dipole-quadrupole external gravitational field can be expressed in cylindrical Weyl coordinates (t, x, ϕ, z) as [29],

$$ds^2 = -V(x, z)dt^2 + x^2V^{-1}(x, z)d\phi^2 + f(x, z)(dx^2 + dz^2), \quad (1)$$

where

$$\begin{aligned} V(x, z) &= \frac{\mu_1\mu_3}{\mu_2\mu_4} \exp\left[2b_1z + 2b_2\left(z^2 - \frac{x^2}{2}\right)\right], \\ f_0(x, z) &= 16C_f \frac{\mu_1^3\mu_2^5\mu_3^3\mu_4^5}{W_{11}W_{22}W_{33}W_{44}W_{13}^2W_{24}^2Y_{12}Y_{14}Y_{23}Y_{34}} \\ &\times \exp\left[-b_1^2x^2 + \frac{b_2^2}{2}(x^2 - 8z^2)x^2 - 4b_1b_2zx^2\right. \\ &+ 2b_1(-z + \mu_1 - \mu_2 + \mu_3 - \mu_4) \\ &+ b_2(-2z^2 + x^2 + 4z(\mu_1 - \mu_2) + \mu_1^2 - \mu_2^2 \\ &\left. + (\mu_3 - \mu_4)(4z + \mu_3 + \mu_4))\right]. \end{aligned} \quad (2)$$

In the above expressions, $W_{ij} = x^2 + \mu_i\mu_j$, $Y_{ij} = (\mu_i - \mu_j)^2$, and $\mu_i = \sqrt{x^2 + (z - w_i)^2} - (z - w_i)$, where (i, j) take values from 1 to 4. The values of w_i are chosen as $w_1 = z_1 - m_1$, $w_2 = z_1 + m_1$, $w_3 = z_2 - m_2$, and $w_4 = z_2 + m_2$. Here, the quantities m_i and z_i denote the mass and position of the i -th black hole, respectively. Additionally, b_1 and b_2 are the dipole and quadrupole momenta of the external gravitational field, respectively, while C_f refers the gauge parameter.

The static and axisymmetric metric (1) is an exact analytical solution of the vacuum Einstein's equations in general relativity. It is important to note that the balance between two sources would be lost when the external gravitational field is absence ($b_1 = b_2 = 0$). In such a scenario, Eq. (1) boils down to the usual Bach-Weyl metric [37–39], which also represents the double Schwarzschild black hole solution. In the binary system (1), two event horizons extend into the regions $w_1 < z < w_2$ and $w_3 < z < w_4$ when $x = 0$, covering the curvature singularities of the spacetime. Moreover, it is not affected by any conical singularities along the z -axis under the regularity condition $f_0V \rightarrow 1$ as $x \rightarrow 0$ [40], which is valid everywhere outside the event horizons of individual

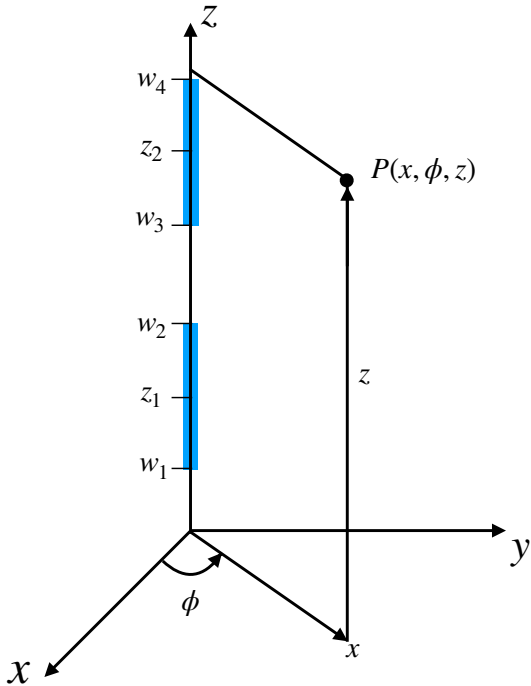


FIG. 1. Schematic diagram of a binary black hole system featuring two co-linear Schwarzschild black holes. The primary and secondary black holes are located at z_1 and z_2 , respectively. The thick blue lines represent the extended regions of the event horizons along the z -axis. For the primary black hole, the horizon extends between w_1 and w_2 , while for the secondary black hole, the horizon extends between w_3 and w_4 . See the text for more details.

sources. To satisfy the equation $f_0 V = 1$, we consider a particular model of the external gravitational background where the parameters C_f , b_1 , and b_2 are expressed in terms of intrinsic black hole parameters (m_1 , m_2 , z_1 , z_2) as [29],

$$\begin{aligned}
 C_f &= 256m_1^2m_2^2(m_1 + m_2 + z_1 - z_2)^2 \\
 &\quad \times (m_1 + m_2 - z_1 + z_2)^2, \\
 b_1 &= -\frac{(m_1z_1 + m_2z_2)}{4m_1m_2(z_1 - z_2)} \\
 &\quad \times \log \left[\frac{(m_1 - m_2 + z_1 - z_2)(m_1 - m_2 - z_1 + z_2)}{(m_1 + m_2 + z_1 - z_2)(m_1 + m_2 - z_1 + z_2)} \right], \\
 b_2 &= \frac{(m_1 + m_2)}{8m_1m_2(z_1 - z_2)} \\
 &\quad \times \log \left[\frac{(m_1 - m_2 + z_1 - z_2)(m_1 - m_2 - z_1 + z_2)}{(m_1 + m_2 + z_1 - z_2)(m_1 + m_2 - z_1 + z_2)} \right]. \tag{3}
 \end{aligned}$$

It is worth pointing out that m_1 , m_2 , z_1 , and z_2 values remain unconstrained, providing a more generic double black hole configuration. In Fig. 1, we display a binary black hole system in coordinates (t, x, ϕ, z) .

To analyze the event horizons of the two sources, we need to consider the near-horizon limit of metric (1).

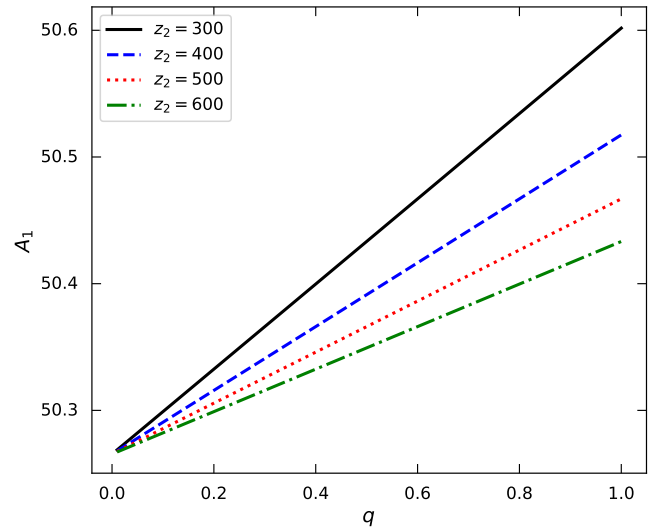


FIG. 2. Plot of horizon area (A_1) of the primary black hole with binary mass ratio (q) for different binary separations $z_2 = 300, 400, 500,$ and 600 . See the text for details.

The near-horizon geometry of the primary black hole has been examined in [29]. In that study, the coordinates transformation $x = \sqrt{r(r - 2m_1)} \sin \theta$ (event horizon at $x_H = 0$) and $z = z_1 + (r - m_1) \cos \theta$ brings the metric (1) into a deformed Schwarzschild metric as r approaches $2m_1$ (see Eq. (11) in [29]). So, it is evident that both the external fields and the secondary black hole can distort the primary black hole horizon. A similar description applies to the secondary black hole as well. Indeed, the binary black hole system (1) contains two distorted Schwarzschild black holes. The horizon area of primary black hole is calculated as [29],

$$\mathcal{A}_1 = 16\pi \frac{1 + q + z_2}{1 - q + z_2} \exp[-2b_1(1 + 2q) - 8b_2qz_2], \tag{4}$$

where $q (= m_2/m_1)$ is defined as the binary mass ratio. In this work, we use a unit system: $G = c = m_1 = 1$, where G is the gravitational constant and c is the speed of light. Also, we place the primary black hole at $z_1 = 0$. In Fig. 2, we illustrate the dependency of A_1 on mass ratio (q) and distance between two sources (z_2), where the variation of A_1 as a function of q for different z_2 values has been displayed. The solid (black), dashed (blue), dotted (red), and dash-dotted (green) curves represent the obtained results for $z_2 = 300, 400, 500,$ and 600 , respectively. We observed that for a given z_2 , A_1 increases with q . However, for a fixed q , A_1 decreases with z_2 . Therefore, q and z_2 play opposite roles in determining the characteristics of A_1 .

III. MODEL EQUATIONS

In this section, we aim to model the transonic accretion flow in the CPD within the stationary and axisymmetric BBH system (1). Hydrodynamics of the CPD are studied within the framework of general relativity [41]. We consider the fluid motion is restricted on the $z = 0$ plane of the central source ($u^z = 0$ and $\partial Q/\partial z = 0$, where Q represents any flow parameter). Additionally, we assume that the flow is steady ($\partial Q/\partial t = 0$), axisymmetric ($\partial Q/\partial \phi = 0$), and inviscid.

A. Governing equations for CPD

The fundamental governing equations that describe the flow motion in the CPD are given by [42],

(a) Radial momentum equation:

$$\gamma_v^2 v \frac{dv}{dx} + \frac{1}{e+p} \frac{dp}{dx} + \left(\frac{d\Phi^{\text{eff}}}{dx} \right)_\lambda = 0, \quad (5)$$

(b) Energy equation:

$$\frac{e+p}{\rho} \frac{d\rho}{dx} - \frac{de}{dx} = 0, \quad (6)$$

where v is the radial-component of the physical three-velocity in the co-rotating frame (CRF, i.e., a frame orbits with the same angular velocity Ω as the fluid) [43, 44], which takes negative values for accretion, and $\gamma_v = 1/\sqrt{1-v^2}$ denotes the Lorentz-factor corresponding to v . Here, ρ is the rest-mass density, e ($= \rho + \Pi$, Π is the internal energy density) is the total energy density, and p is the isotropic pressure of the flow. The quantity Φ^{eff} is called the effective potential of the accreting system, and it is obtained as,

$$\Phi^{\text{eff}} = 1 + \frac{1}{2} \ln \left[\frac{x^2 V}{x^2 - \lambda^2 V^2} \right], \quad (7)$$

where λ ($= -u_\phi/u_t$, u_ϕ and u_t denote the ϕ and t components of the covariant four-velocity u_k , respectively) is the specific angular momentum of the flow. Note that in the energy equation (6), we do not consider any radiative cooling processes due to the low mass accretion rate of the supermassive black holes [45, 46].

From the time translation and azimuthal symmetries of the spacetime, we derive two conserved quantities along the stream lines of flow:

$$E = -\frac{e+p}{\rho} u_t, \quad \mathcal{L} = \frac{e+p}{\rho} u_\phi, \quad (8)$$

where E is known as the Bernoulli constant and \mathcal{L} represents the bulk angular momentum per unit mass. Therefore, λ ($= \mathcal{L}/E$) remains conserved along the flow direction. Using the normalization condition ($u^k u_k = -1$) of

the four-velocity, we determine u_t as,

$$u_t = -\gamma_v \sqrt{\frac{V}{1-\Omega\lambda}}, \quad (9)$$

where Ω ($= u^\phi/u^t = \lambda V^2/x^2$) refers the angular velocity of the flow.

The mass accretion rate of the flow is derived by integrating the continuity equation $\nabla_k(\rho u^k) = 0$, and it is given by,

$$\dot{M} = -4\pi\rho H v \gamma_v \sqrt{f_0}, \quad (10)$$

where H is the local half-thickness of the disc. The expression of H is obtained by considering the hydrodynamic equilibrium along the transverse direction of the disc as [44, 47, 48],

$$H = \sqrt{\frac{px^3}{\rho F}}, \quad F = \frac{1}{1-\Omega\lambda}. \quad (11)$$

To solve the dynamical equations of the flow, we require an equation of state (EoS) that relates various thermodynamic quantities of the flow. We assume the fluid system consists of fully ionized plasma, which means fluid satisfies the charge neutrality condition $n_p = n_e \approx \rho/m_p$, where n_p and n_e represent the number densities of protons and electrons, respectively. Since for hot accretion flow (HAF), the plasma temperature can reach up to $\sim 10^{10-12}\text{K}$ [46] near the horizon, we employ the relativistic EoS with variable adiabatic index Γ , as proposed in [49]. Accordingly, the internal energy density e and isotropic pressure p are defined as,

$$e = \frac{\rho f}{1+m_p/m_e}, \quad p = \frac{2\rho\Theta}{1+m_p/m_e}, \quad (12)$$

where m_p and m_e are masses of proton and electron, respectively, and $\Theta [= k_B T/(m_e c^2)$, k_B is the Boltzmann constant and T is the flow temperature in Kelvin] is the dimensionless temperature. Here, the quantity f is given by,

$$f = 1 + \frac{m_p}{m_e} + \Theta \left[\left(\frac{9\Theta + 3}{3\Theta + 2} \right) + \left(\frac{9\Theta + 3m_p/m_e}{3\Theta + 2m_p/m_e} \right) \right]. \quad (13)$$

Integrating Eq. (6) by using Eqs. (12) and (13), the expression of mass density ρ in terms of Θ is calculated as,

$$\rho = \mathcal{K} \exp(\chi) \Theta^{3/2} (3\Theta + 2)^{3/4} (3\Theta + 2m_p/m_e)^{3/4}, \quad (14)$$

where \mathcal{K} is the entropy constant and $\chi = (f - 1 - m_p/m_e)/(2\Theta)$. We determine the entropy accretion rate, which is also a constant of motion due to the adiabatic nature of the flow, and is given by [50, 51],

$$\dot{\mathcal{M}} = \frac{\dot{M}}{4\pi\mathcal{K}} = -v\gamma_v H \sqrt{f_0} \exp(\chi) \times \Theta^{3/2} (3\Theta + 2)^{3/4} (3\Theta + 2m_p/m_e)^{3/4}. \quad (15)$$

In the steady state, \dot{M} is typically treated as a constant of motion. Therefore, we solve the equation $d\dot{M}/dx = 0$ with the help of Eqs. (6) and (12) which yields the temperature gradient as,

$$\frac{d\Theta}{dx} = -\frac{2\Theta}{2N+1} \left[\frac{\gamma_v^2}{v} \frac{dv}{dx} + N_{11} + N_{12} \right], \quad (16)$$

with

$$N_{11} = \frac{3}{2x} - \frac{1}{2F} \frac{dF}{dx}, \quad N_{12} = \frac{1}{2f_0} \frac{df_0}{dx}, \quad (17)$$

where $N (= \frac{1}{2} \frac{df}{d\Theta})$ refers the polytropic index.

Subsequently, by solving Eqs. (5), (6), (12), and (16), we derive the radial-velocity gradient as,

$$\frac{dv}{dx} = \frac{\mathcal{N}}{\mathcal{D}}. \quad (18)$$

The expressions of numerator (\mathcal{N}) and denominator (\mathcal{D}) are given by,

$$\mathcal{N} = \frac{2C_s^2}{\Gamma+1} (N_{11} + N_{12}) - \frac{d\Phi^{\text{eff}}}{dx}, \quad (19)$$

$$\mathcal{D} = \gamma_v^2 \left[v - \frac{2C_s^2}{(\Gamma+1)v} \right], \quad (20)$$

where $C_s (= \frac{\Gamma p}{e+p} = \frac{2\Gamma\Theta}{f+2\Theta})$ is the adiabatic sound speed.

B. Conditions for critical point

In case of transonic accretion flow, it must cross the event horizon (x_H) with radial velocity close to the speed of light ($v \approx 1$), thereby satisfying the inner boundary condition at the event horizon [27, 28]. Usually, accreting matter begins its journey with negligible radial velocity ($v \ll 1$) at the outer edge of the accretion disc. As the flow moves inward, it must pass through at least one critical point (x_c) where it changes the sonic state from subsonic to supersonic. At x_c , the radial velocity gradient takes the indeterminate form $(dv/dx)_{x_c} = 0/0$. Therefore, for the critical points, we find the following conditions:

$$\mathcal{N} = \mathcal{D} = 0. \quad (21)$$

To calculate the real and finite values of $(dv/dx)_{x_c}$, we apply l'Hôpital's rule to Eq. (18). We obtain two distinct values of $(dv/dx)_{x_c}$, and depending on them, critical points are classified into three categories: saddle, nodal, and spiral types. If both values of $(dv/dx)_{x_c}$ are real with opposite sign, the critical point is called as a saddle-type critical point. For a nodal-type critical point, $(dv/dx)_{x_c}$ values are real and have same sign. When $(dv/dx)_{x_c}$ is imaginary, the critical point is classified as a spiral-type critical point. It is noted that a positive value of

$(dv/dx)_{x_c}$ yields the accretion solution, while a negative value of $(dv/dx)_{x_c}$ gives the wind solution. In this work, we focus only on the accretion solutions, leaving the wind solutions for future study. Additionally, among the various types of critical points, saddle-type critical points are physically acceptable. Therefore, we concentrate on the accretion solutions that only pass through the saddle-type critical points. We further point out that the flow can have single or multiple critical points depending on the model parameters. A detailed analysis of the critical points is discussed in Section IV A.

The above equations are essential for determining the accretion solutions and their associated thermodynamic flow variables. In this study, we also aim to explore the spectral characteristics of the accretion solutions in terms of emissivity, luminosity distribution, and optical depth, etc. The required model equations for this analysis are presented in the following section.

C. Radiative properties of accretion flow

We consider the relativistic thermal bremsstrahlung (free-free) emission from the CPD. For HAF, electron-electron emission dominates over electron-ion emission [52], and hence we use an approximate expression for the free-free emissivity, given by [53],

$$\begin{aligned} \mathcal{E}_{\nu_e}^{\text{ff}} &= \frac{32\pi e^6}{3m_e m_p^2 c^3} \sqrt{\frac{2\pi}{3m_e k_B}} Z^2 \rho^2 T_e^{-1/2} (1 + 4.4 \times 10^{-10} T_e) \\ &\times \exp\left(-\frac{h\nu_e}{k_B T_e}\right) \bar{g}_{\text{ff}} \text{ erg s}^{-1} \text{ cm}^{-3} \text{ Hz}^{-1}, \end{aligned} \quad (22)$$

where Z represents the atomic number of the ion, which is taken as 1 for the hydrogen plasma, h is the Planck constant, and ν_e is the emission frequency. The term \bar{g}_{ff} denotes the thermally-averaged Gaunt factor, which does the quantum mechanical correction to the classical electrodynamics. Its value varies between 1 to 5, depending on the electron energy. However, following [45], we take $\bar{g}_{\text{ff}} = 1.2$ throughout this paper. Note that the second term in Eq. (22) includes both the relativistic corrections and electron-electron bremsstrahlung emission. Also, we assume a weak coupling between the electrons and ions, which leads to a temperature difference between them. There are many studies in the literature corresponding to the two-temperature accretion flows [54–58]. However, in accordance with [45], we use a simplified parameterized relation $T_e = T/10$.

The emission coefficient of accretion flow, as described in Eq. (22), is measured locally. However, for an observer at spatial infinity, this radiation must be red-shifted due to both the gravitational potential of the black hole and the Doppler effect resulting from the rotation of the disc.

Here, we do not consider the light bending effect to the photons for simplicity. Also, the disc inclination angle with respect to the line of sight of the observer is taken as 45° [52, 59, 60]. Under these assumptions, the observed frequency ν_o is obtained in terms of the emitted frequency ν_e as [61],

$$\nu_o = \frac{\nu_e}{1+z} = \frac{\nu_e}{u^t \left(1 + \frac{r\Omega}{\sqrt{2}c} \sin \phi\right)}, \quad (23)$$

where $(1+z)$ is the red-shift factor. The expression of u^t is calculated from Eq. (9), and is given by,

$$u^t = \frac{\gamma v}{\sqrt{(1-\Omega\lambda)V}}. \quad (24)$$

Using Eqs. (22) and (23), we get the monochromatic luminosity of the CPD at a observed frequency ν_o as,

$$\begin{aligned} L_{\nu_o} &= 2 \int_{x_0}^{x_{\text{edge}}} \int_0^{2\pi} \mathcal{E}_{\nu_e}^{\text{ff}} H x dx d\phi \\ &= \frac{64\pi e^6}{3m_e m_p^2 c^3} \sqrt{\frac{2\pi}{3m_e k_B}} \bar{g}_{\text{ff}} \int_{x_0}^{x_{\text{edge}}} \int_0^{2\pi} \left[H x \rho^2 T_e^{-1/2} \right. \\ &\quad \times (1 + 4.4 \times 10^{-10} T_e) \exp\left(-\frac{(1+z)h\nu_o}{k_B T_e}\right) \left. \right] dx d\phi \\ &\quad \times \text{erg s}^{-1} \text{ Hz}^{-1}, \end{aligned} \quad (25)$$

where x_0 ($= x_H =$ event horizon radius) and x_{edge} are the inner and outer edges of the CPD, respectively.

Bremsstrahlung radiation can only be observed when the emitting medium is optically thin; otherwise, photons will be destroyed through true absorption after undergoing multiple coherent scattering. The primary source of opacity is the Thomson scattering by the free electrons with opacity coefficient $\kappa_s = 0.4 \text{ cm}^2 \text{ gm}^{-1}$ [62]. In a fully ionized medium, free-free absorption also significantly contributes to the photon opacity [62]. Using Eq. (22), we calculate the Rosseland mean opacity coefficient for the free-free absorption as [63],

$$\begin{aligned} \kappa_{\text{R}}^{\text{ff}} &= 0.64 \times 10^{23} \rho T_e^{-7/2} \\ &\quad \times (1 + 4.4 \times 10^{-10} T_e) \bar{g}_{\text{ff}} \text{ cm}^2 \text{ gm}^{-1}. \end{aligned} \quad (26)$$

Here, we consider the typical length scale of the medium is the half-thickness (H) of the disc. Therefore, the effective optical depth of the disc is obtained by considering the aforementioned opacity sources as [64],

$$\tau_{\text{eff}} \approx \sqrt{\tau_a(\tau_a + \tau_s)}, \quad (27)$$

where τ_s ($= \kappa_s \rho H$) is the scattering optical depth and τ_a ($= \kappa_{\text{R}}^{\text{ff}} \rho H$) is the absorption optical depth.

With these useful equations, we present the results regarding the accretion properties of the CPD in the subsequent sections.

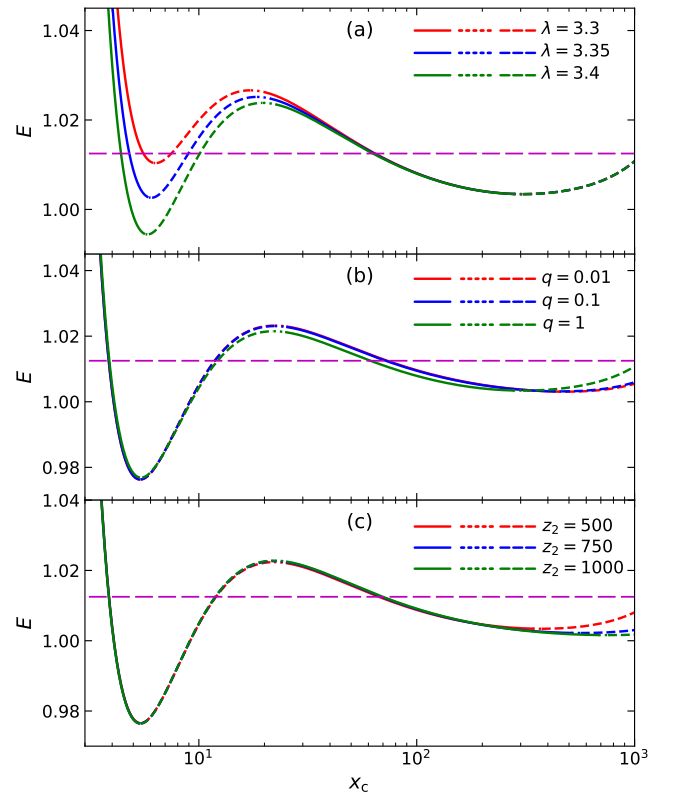


FIG. 3. Plot of specific energy (E) as a function of critical point location (x_c) for different angular momentum (λ) in panel (a), binary mass ratio (q) in panel (b), and binary separation (z_2) in panel (c). Here, solid, dotted, and dashed curves represent saddle, nodal, and spiral types critical points, respectively. The horizontal dashed lines (magenta) denote the energy values where the flow possesses multiple critical points. See the text for details.

IV. RESULTS

A. Analysis of critical points

We already pointed out that the transonic accretion flow must pass through the critical points; therefore, we start our analysis by investigating how the behaviors of critical points depend on different global constants, such as specific angular momentum (λ), binary mass ratio (q), and binary separation (z_2). To do this, we first compute the flow temperature (Θ_c) and radial velocity (v_c) at a critical point (x_c) for a given set of input parameters (λ, q, z_2) by solving the critical point conditions (21). Subsequently, using these results in Eq. (8), we calculate the specific energy (E) at x_c for the same set of input parameters mentioned above. The obtained results are shown in Fig. 3, where the variation of E as a function of x_c is illustrated. In panel (a), we fix $(q, z_2) = (1, 500)$ and vary the angular momentum as $\lambda = 3.3, 3.35$, and 3.4 . In panel (b), we set $(\lambda, z_2) = (3.5, 500)$ and vary

TABLE I. Binary mass ratio (q), binary separation (z_2), inner critical point (x_{in}), outer critical point (x_{out}), and terminate radius (x_t) for accretion solutions presented in Fig. 4.

q	z_2	x_{in}	x_{out}	x_t
0.01	500	3.8899	95.5954	36.6399
0.1	500	3.8924	93.8551	37.1224
1	500	3.9180	78.4602	44.5380
0.5	500	3.9038	86.5751	39.7038
0.5	750	3.8990	88.8785	38.5990
0.5	1000	3.8967	90.2864	38.0367

the mass ratio as $q = 0.01, 0.1$, and 1 . Finally, in panel (c), we choose $(\lambda, q) = (3.5, 0.5)$ and vary the binary separation as $z_2 = 500, 750$, and 1000 . The color codes corresponding to the different input parameters are indicated in each panel. In each curve, the saddle, nodal, and spiral-type critical points are represented by solid, dotted, and dashed lines, respectively. We observe that the flow energy remains constant in all cases when the critical points are located at large distances from the black hole. However, the flow energy changes significantly when the critical points are closer to the black hole. For each curve, the critical points are formed in a systematic order as saddle-nodal-spiral-nodal-saddle-spiral when the critical points move toward the outer edge of the disk. Moreover, we observe that the flow energy changes moderately with an increase in λ . However, it shows small variation with increases in q and z_2 . Interestingly, a broad range of energy values exists where the flow possesses two saddle-type critical points (as indicated by the horizontal dashed lines (magenta) in all the panels). It is important to note that such regions with multiple critical points are of particular interest in the study of shock-induced accretion solutions. For the shock scenarios [42, 60, 65–68], a global solution can pass through both the inner (i.e., formed near the black hole) and outer (i.e., formed far from the black hole) critical points, provided that the relativistic shock conditions are satisfied. A detailed analysis of the shock solutions is presented in Section IV C.

B. Effect of binary parameters on the transonic accretion solutions

In this section, we aim to investigate the effect of the secondary black hole (SBH) on the accretion solutions in the CPD. To determine the transonic accretion solutions, we calculate the critical point x_c and its corresponding flow variables v_c and Θ_c for a given set of input parameters (q, z_2, λ, E) by using Eqs. (21) and (8). Next, using the calculated parameters (Θ_c, v_c) at x_c as the initial boundary conditions, we first integrate Eqs. (16) and (18) from x_c to the disc inner edge x_0 , and then from x_c

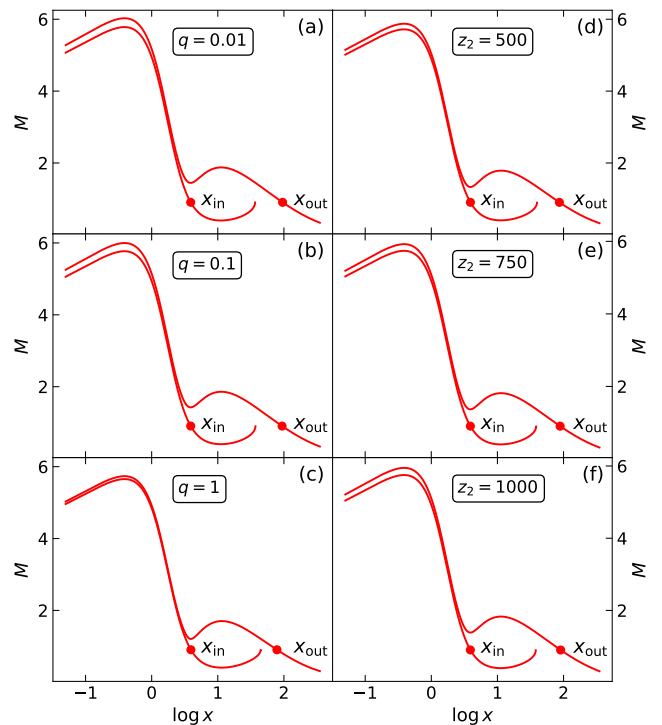


FIG. 4. Plot of Mach number ($M = v/C_s$) as a function of radial distance (x) for the binary mass ratio $q = 0.01, 0.1$, and 1 with binary separation $z_2 = 500$ (left panels), and for $z_2 = 500, 750$, and 1000 with $q = 0.5$ (right panels). Here, the critical points are marked by the filled circles, and we choose $\lambda = 3.5$ and $E = 1.01$. See the text for details.

to the disc outer edge x_{edge} . Finally, by combining both segments of the solutions, we obtain the resulting global accretion solution corresponding to the same set of input parameters (q, z_2, λ, E) . In this work, the inner and outer edges of the accretion disc are taken as $x_0 = 0.05$ and $x_{\text{edge}} = 350$, respectively. It is essential to mention that there is no qualitative difference in the characteristics of the accretion solutions if the inner edge position is chosen more closer to the horizon ($x_{\text{H}} = 0$) instead of $x_0 = 0.05$. In Fig. 4, we depict the typical accretion solutions (i.e., variation of the Mach number ($M = v/C_s$) as a function of the radial coordinate (x)) for different values of q and z_2 . Here, we choose the input flow parameters as $\lambda = 3.5$ and $E = 1.01$. The left panels represent the accretion solutions corresponding to the mass ratio $q = 0.01, 0.1$, and 1 with binary separation $z_2 = 500$. Similarly, the right panels denote the accretion solutions for $z_2 = 500, 750$, and 1000 with $q = 0.5$. In all cases, the solutions that pass through the outer critical points (x_{out}) are globally extended from x_{edge} to x_0 . In contrast, the solutions that pass through the inner critical points (x_{in}) are truncated at certain radii (x_t) in between x_{in} and x_{out} . Accretion solutions of this kind are usually referred as A-type solutions [42, 52, 59, 60, 66, 68]. Interestingly, for A-type

solution topology, the solution that passes through x_{out} may connect to the solution that passes through x_{in} via a standing shock transition, as the inner solution branch has a higher entropy content than the outer one [69]. The shock-induced accretion solutions will be examined later in Section IV C. It is evident from the figure that the nature of the accretion solutions does not change with an increase in either of the binary parameters q and z_2 . The positions of the critical points associated with these accretion solutions are summarized in Table I. This table shows that x_{in} increases, while x_{out} decreases as q increases at a given z_2 . On the other hand, when z_2 increases at a fixed q , x_{in} and x_{out} move oppositely compared to the previous case.

C. Physical properties of the CPD with shock

In this section, we focus on studying the effect of binary parameters (q, z_2) on the shock-induced accretion solutions and examine their corresponding physical properties. In Fig. 5a, we present the dynamical structure of the shock solutions for different values of mass ratio (q) with binary separation $z_2 = 350$, where the Mach number (M) is plotted as a function of radial distance (x). Here, we choose $\lambda = 3.45$ and $E = 1.01$. The solid curves with black, blue, red, and green colors denote the shock solutions for $q = 0.25, 0.5, 0.75$, and 1 , respectively. However, the dashed curves with the same color code represent the respective shock-free solutions. The locations of the critical points ($x_{\text{in}}, x_{\text{out}}$) and shock radius (x_{sh}) for these shock solutions are tabulated in Table II. In a general scenario, the accretion solution, after passing through the outer critical point x_{out} , continues to move toward the central black hole until it crosses the event horizon (see the dashed curves). Meanwhile, the flow slows down when the centrifugal repulsion due to flow rotation becomes dominant against the gravitational pull of the central black hole. Consequently, this supersonic flow jumps into the subsonic branch, which contains x_{in} . Thereafter, the flow becomes supersonic once more after crossing x_{in} , and continues to accrete toward the horizon. Therefore, in the shock scenario, the accretion solution can pass through both x_{in} and x_{out} via a discontinuous jump in between them. To calculate the shock location, we use the following relativistic shock conditions which are given by [70],

- (a) Mass flux conservation: $[\rho u^x]$,
- (b) Energy flux conservation: $[(e + p)u^x u^t]$,
- (c) Radial-momentum flux conservation:
 $[(e + p)u^x u^x + pg^{xx}]$,

where the quantities with the square bracket denote the difference of their values across the shock front. Us-

ing these shock conditions, we calculate the shock locations at $x_{\text{sh}} = 19.8524, 20.9639, 22.2453$, and 23.7268 for $q = 0.25, 0.5, 0.75$, and 1 , respectively, as indicated by the solid vertical lines. It is observed that the shock location moves away from the horizon as the mass ratio increases. In the respective panels (b)–(f) of Fig. 5, we present the profiles of radial-velocity (v), mass density (ρ), electron temperature (T_e), frequency-integrated emissivity (\mathcal{E}), and effective optical depth (τ_{eff}) for both shock-free and shock-induced accretion solutions in Fig. 5a. In this work, we consider a SMBHB with the primary black hole mass $m_1 = 10^6 M_\odot$, where M_\odot is the Solar mass. The mass accretion rate of the flow is taken as $\dot{M} = 10^{-5} \dot{M}_{\text{Edd}}$, where $\dot{M}_{\text{Edd}} = 1.39 \times 10^{18} m_1 / M_\odot \text{ gm s}^{-1}$ is the Eddington mass accretion rate. We observed that all the analyzed quantities significantly change at the shock locations. Moreover, the differences in these quantities across the shock fronts diminish as the mass ratio increases. This result is expected because the shock fronts settle at larger radii as the mass ratio increases. Since the radial velocity drops down at the shock radius, according to the conservation of the mass flux across the shock front (see the shock condition (a)), the mass density of the post-shock corona (hereafter PSC) increases. After the shock transition, the kinetic energy of the post-shock flow is converted into the thermal energy, leading to an increase in the electron temperature of the PSC. It is important to note that the soft photons emitted by the pre-shock disk may undergo inverse Compton scattering by the swarm of hot electrons in the PSC, resulting in the production of high-energy radiations [11]. We also observe that the emissivity of the radiation in the PSC is greater than that in the pre-shock disk due to the higher mass density and electron temperature of the flow in the PSC compared to the pre-shock disk. Furthermore, we find that the effective optical depth of the accretion disk is substantially low, even in the case of shock solutions. As a result, the disk remains optically thin, allowing the photons to escape the medium before being absorbed by the accretion disk.

Similarly, for a fixed mass ratio $q = 0.5$ and varying binary separation z_2 , we present the typical shock solutions in Fig. 6a. The corresponding flow variables such as the radial-velocity (v), mass density (ρ), electron temperature (T_e), frequency-integrated emissivity (\mathcal{E}), and effective optical depth (τ_{eff}) are shown in Figs. 6b–f, respectively. The obtained results are denoted by the solid lines with black, blue, red, and green colors for $z_2 = 300, 400, 500$, and 600 , respectively. The shock-free solutions corresponding to the same set of input parameters are shown by the dashed curves with the same color codes as those used for the shock-induced solutions. For $z_2 = 300, 400, 500$, and 600 , we obtain the shock locations at $r_{\text{sh}} = 21.2977, 20.711, 20.3470$, and 20.1043 , respectively. We observe that for a given q , the shock radius decreases with z_2 . As a result, the change in flow

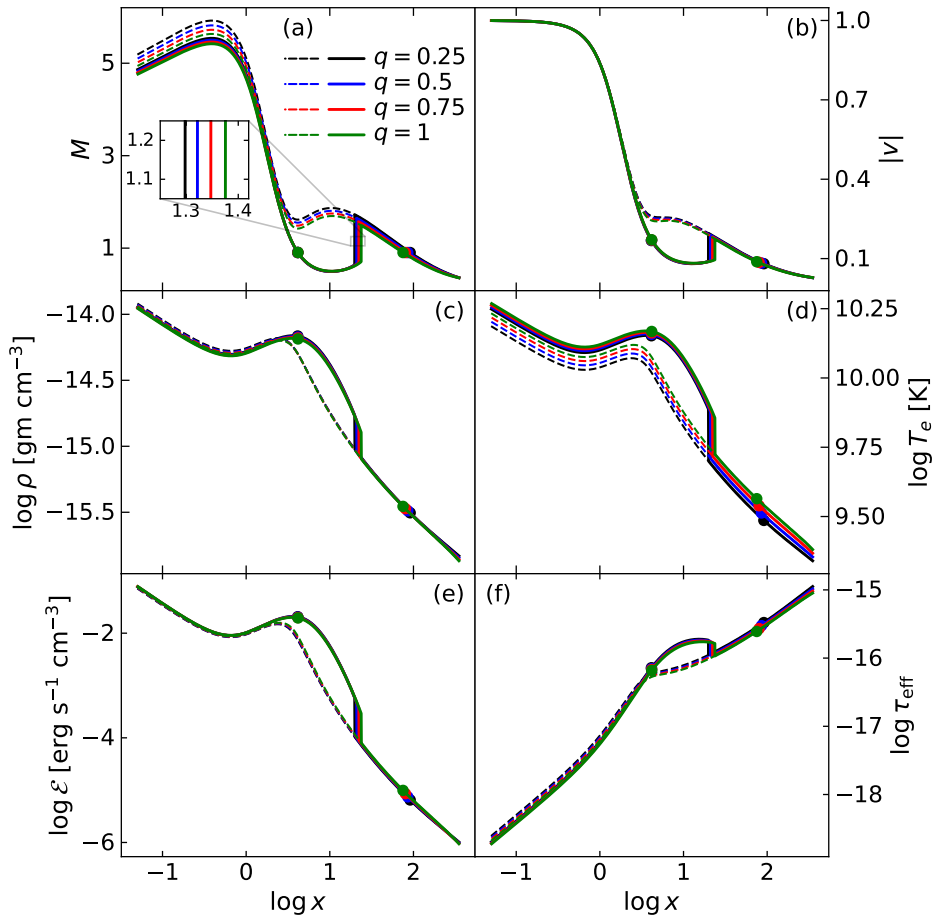


FIG. 5. Illustration of the shock-induced accretion solutions (Mach number (M) versus radial distance (x) curves (solid) in panel (a) for binary mass ratios $q = 0.25, 0.5, 0.75$, and 1 with binary separation $z_2 = 350$. The respective profiles of radial-velocity (v) in panel (b), mass density (ρ_0) in panel (c), electron temperature (T_e) in panel (d), frequency-integrated emissivity (\mathcal{E}) in panel (e), and effective optical depth (τ_{eff}) in panel (f). The dashed curves denote the scenario where shock transitions have not occurred. The flow parameters for this figure are chosen as $\lambda = 3.45$ and $E = 1.01$. See the text for details.

TABLE II. Binary mass ratio (q), binary separation (z_2), inner critical point (x_{in}), outer critical point (x_{out}), and shock location (x_{sh}) for shock-induced accretion solutions presented in Fig. 5.

q	z_2	x_{in}	x_{out}	x_{sh}
0.25	350	4.1324	91.3261	19.8524
0.5	350	4.1439	85.5283	20.9639
0.75	350	4.1553	80.0888	22.2453
1	350	4.1668	75.0221	23.7268
0.5	300	4.1477	85.2372	21.2977
0.5	400	4.1410	86.0856	20.7110
0.5	500	4.1370	87.2893	20.3470
0.5	600	4.1343	88.3404	20.1043

variables across the shock front increases. Here, the flow remains optically thin throughout the disc; hence, the

bremstrahlung radiation can be emitted from the accretion disc without lost its information.

Now, we investigate the spectral energy distribution (SED) of the CPD by considering the emission of thermal bremsstrahlung radiation from the accretion disc. We calculate the SED for the accretion solutions presented in Figs. 5 and 6 using Eq. (22). The results are shown in Figs. 7a-b, respectively, where the variation of the quantity $\nu_o L_{\nu_o}$ with the observed frequency ν_o is depicted. In both panels, we observe that the emitted radiation reaches its maximum power at $\nu_o \approx 10^{20}\text{Hz}$ [45]. Since the electron temperature at the inner edge of the disc is $T_{e0} \approx 10^{10}\text{K}$, the spectra exhibit a cutoff at $\nu_o \approx 10^{21}\text{Hz}$ ($= k_B T_{e0}/h$) [53]. It is also found that the SEDs for the shock solutions are higher than those for the shock-free solutions [68]. This occurs because the temperature distribution in the disc for a shock solution is higher, particularly in the PSC, compared to that in a shock-free solution. Furthermore, across the

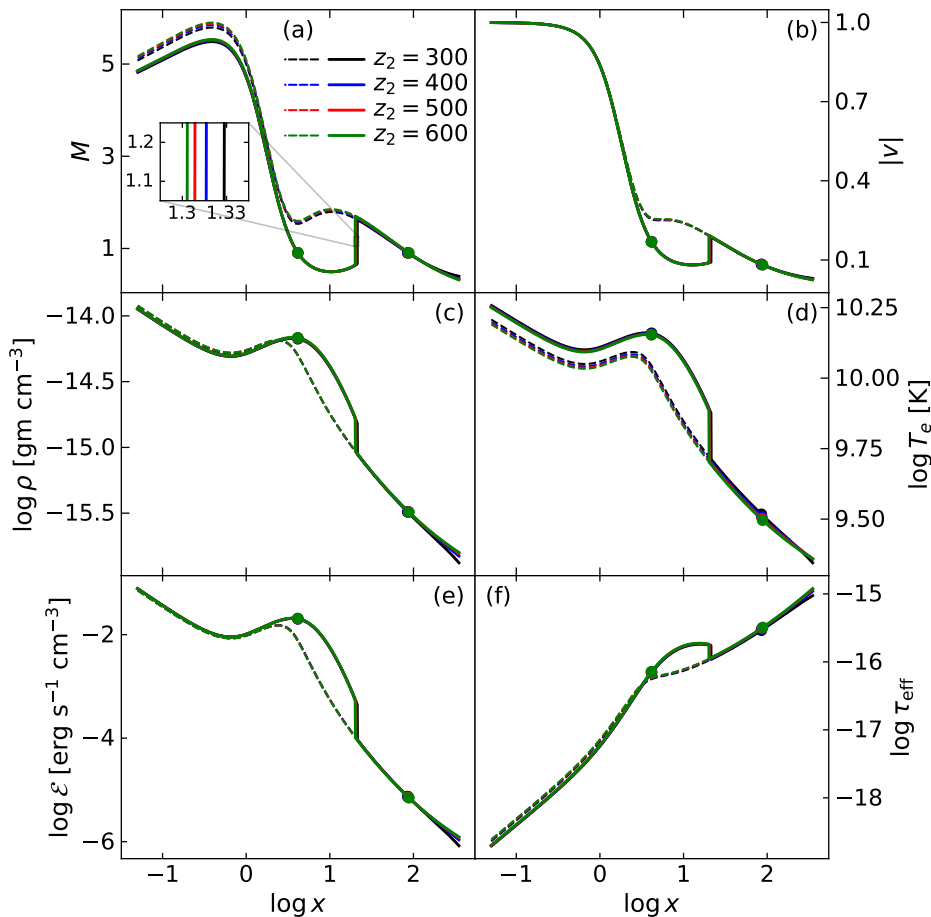


FIG. 6. Typical shock solutions (Mach number (M) versus radial distance (x) curves (solid) in panel (a) for binary separations $z_2 = 300, 400, 500,$ and 600 with mass ratio $q = 0.5$. The profiles of radial-velocity (v), mass density (ρ), electron temperature (T_e), frequency-integrated emissivity (\mathcal{E}), and effective optical depth (τ_{eff}) are depicted in panels (b)-(f), respectively. The dashed curves represent the situations in which shock transitions have not occurred. In this figure, we choose $\lambda = 3.45$ and $E = 1.01$. See the text for details.

entire frequency domain, the CPD spectra show negligible dependence on the binary parameters q and z_2 for both the shock-induced and shock-free solutions. This is because the electron temperature of the CPD is minimally affected by q and z_2 (see Figs. 5d and 6d). It is important to note that the spectral analysis of the CBD under irradiation from two mini discs was investigated in [19]. In that study, the authors demonstrated that the CBD spectrum is almost independent of the binary mass ratio. However, in our study, we obtain similar results regarding the binary mass ratio by analyzing the CPD spectrum instead of the CBD spectrum.

D. Shock properties of the CPD

Next, we examine the shock properties in terms of the binary parameters q and z_2 . To do this, we calculate the shock radius (r_{sh}) as a function of q for different values of

z_2 . The obtained results are presented in Fig. 8a, where the solid (black), dashed (blue), dotted (red), and dash-dotted (green) curves correspond to $z_2 = 250, 500, 750,$ and 1000 , respectively. In this case, the input parameters are chosen as $\lambda = 3.5$ and $E = 1.01$. We observe that the shock radius recedes away from the black hole as q increases, irrespective of the value of z_2 . Moreover, the shock disappears when q exceeds a critical value, as the shock conditions are no longer satisfied beyond that limit. Also, for a given q , the shock radius decreases when z_2 increases. Since both the density and temperature of the flow undergo significant changes at the shock location, it is essential to study their variations across the shock locations. To examine the density compression, we define a quantity, which is called the compression ratio as $R = \Sigma_+/\Sigma_-$, where “+” and “-” denote the post-shock and pre-shock values of the surface density Σ ($= 2\rho H$). Following Eq. (10), we find an expression of R in terms of flow radial 3-velocity (v) and its Lorentz factor (γ_v)

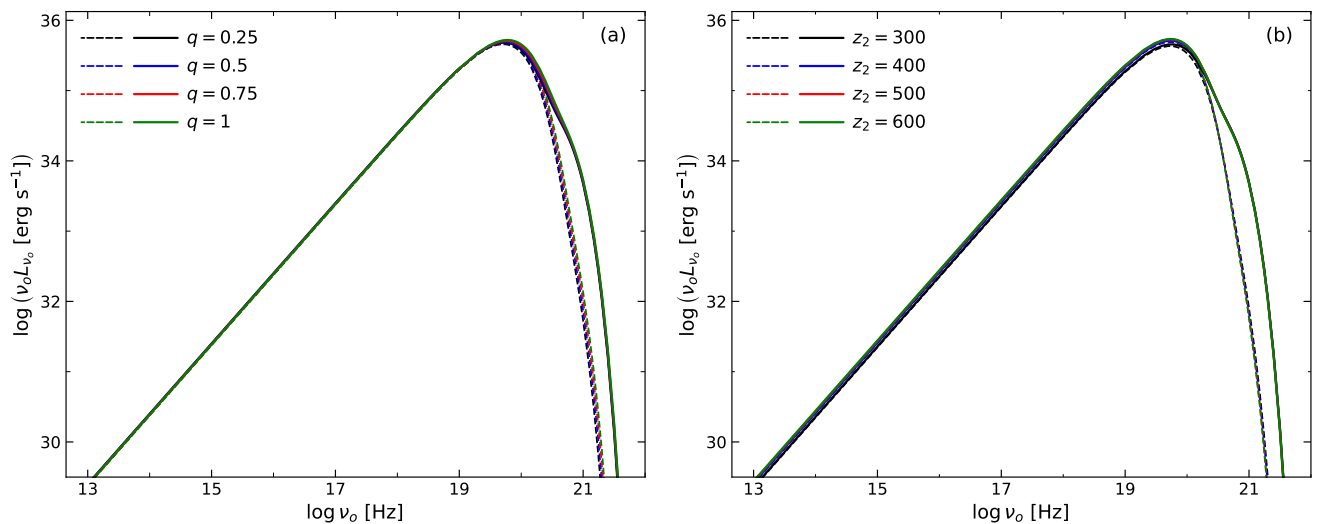


FIG. 7. Spectral energy distribution (i.e., $\nu_o L_{\nu_o}$ versus ν_o curves) of the emitted radiation from the CPD. In panels (a) and (b), the SEDs are presented for the accretion solutions in Figs. 5 and 6, respectively. Here, we choose the set of input parameters as $r_0 = 0.05$, $r_{\text{edge}} = 350$, $\lambda = 3.45$, $E = 1.01$, $m_1 = 10^6 M_\odot$, and $\dot{M} = 10^{-5} \dot{M}_{\text{Edd}}$. See the text for details.

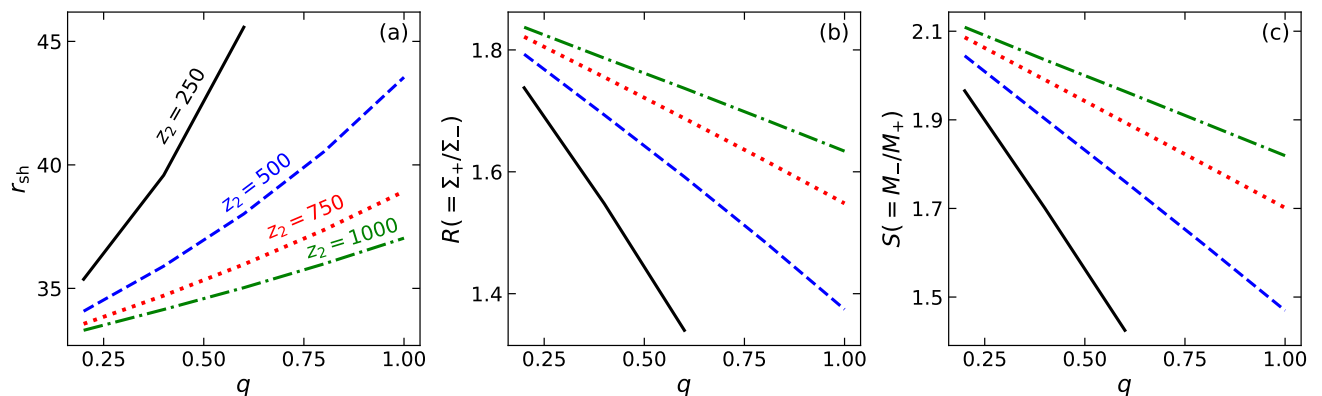


FIG. 8. Variation of shock location (r_{sh}) in panel (a), compression ratio (R) in panel (b), and shock strength (S) in panel (c) as a function of the mass ratio (q) for different binary separations $z_2 = 250, 500, 750,$ and 1000 . In this figure, we set $\lambda = 3.5$ and $E = 1.01$. See the text for details.

as $R = (v\gamma_v)_- / (v\gamma_v)_+$. In Fig. 8b, we present the variation of R with q for the same set of input parameters used in Fig. 8a. It is observed that R decreases with q for a given value of z_2 , which is expected, as the shock locations shift to larger radii when q increases. Since the Mach number (M) depends on the flow temperature (Θ), the temperature jump at the shock front is characterized by a quantity called the shock strength (S). It is defined as the ratio of the pre-shock Mach number (M_-) to the post-shock Mach number (M_+) as $S = M_- / M_+$. In Fig. 8c, we show the variation of S with q . As the shock radius increases with q , it is again expected that S decreases as q increases. Furthermore, for a fixed q , both R and S increase with z_2 as r_{sh} shrinks with z_2 . It is noted that the dependencies of the shock location, density compression, and temperature compression on both q and z_2 are

consistent with the results presented in Figs. 5 and 6.

E. $E - \lambda$ parameter space for shock solutions

We mention earlier that the A-type solutions can harbor shock transitions, provided the relativistic shock conditions are satisfied. Most importantly, shock solutions are not unique but rather have an energy range for a given angular momentum (see Section IV A). Here, we explore the available parameter space for shock solutions in the CPD and see the modification of those identified regions with the mass ratio (q) and binary separation (z_2). For this, we calculate an effective region of the parameter space in the specific angular momentum (λ) and energy (E) plane for a given combination of q and z_2 that admits

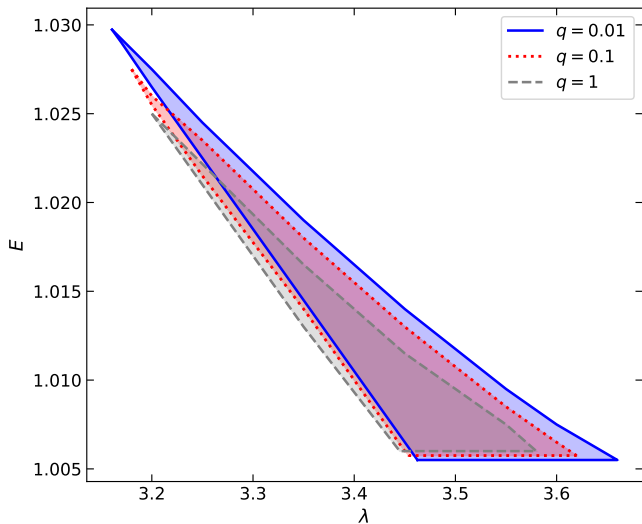


FIG. 9. Modification of the shock parameter space in the specific angular momentum (λ) and energy (E) plane for the mass ratios $q = 0.01, 0.1$, and 1 . In this figure, we choose $z_2 = 300$. See the text for details.

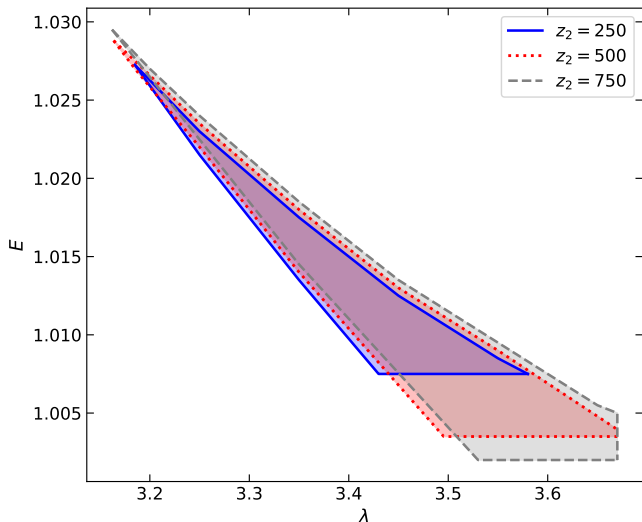


FIG. 10. Modification of the shock parameter space in the $\lambda - E$ plane for the binary separations $z_2 = 250, 500$, and 750 . In this figure, we choose $q = 0.5$. See the text for details.

shock solutions. In Fig. 9, we present the modification of the shock parameter space for different values of q with a fixed $z_2 = 300$. The regions bounded by the solid (blue), dotted (red), and dashed (gray) curves correspond to the results for $q = 0.01, 0.1$, and 1 , respectively. We observed that, the parameter space shifts toward lower λ and lower E domains as q increases. Moreover, the area under the parameter space gradually decreases when the mass of the secondary black hole becomes comparable to that of the primary black hole. Similarly, in Fig. 10, we show the modification of the shock parameter space in the $\lambda - E$

plane as a function of z_2 with a fixed $q = 0.5$, where the effective regions bounded by the solid (blue), dotted (red), and dashed (gray) are obtained for $z_2 = 250, 500$, and 750 , respectively. It is observed that as z_2 increases, the parameter space shifts toward higher λ and lower E sides. In addition, the shock parameter space expands as the secondary black hole moves farther away from the primary one.

V. CONCLUSIONS

In this work, we study the accretion flow properties of the circumpolar disc (CPD) in a binary black hole system. We derive the model equations for general relativistic accretion flow in the background of a binary black hole spacetime. These equations are solved numerically to obtain the transonic accretion solutions both in presence and absence of shocks. Since the secondary black hole can influence the horizon area of the primary black hole, the main objective of this work is to examine the impact of the secondary black hole, mainly its mass and distance with respect to the primary black hole, on the accretion properties of the CPD.

We find that flow may possess single or multiple critical points depending on the specific angular momentum (λ), energy (E), binary mass ratio (q), and binary separation (z_2). We obtain the A-type accretion solutions that contain multiple critical points and show that the behaviors of the accretion solution solutions remain A-type with an increase of both q and z_2 . Since the A-type accretion solutions can exhibit standing shock transitions, provided the relativistic shock conditions are satisfied, we also investigate the shock-induced accretion solutions. We analyze the shock properties such as shock radius (r_{sh}), compression ratio (R), and shock strength (S) as functions of q and z_2 . We observe that as q increases, both R and S decreases as r_{sh} moves away from the horizon. However, as z_2 increases, r_{sh} decreases, resulting in higher values of R and S . We further investigate the luminosity distribution of the CPD as a function of q and z_2 . We find that the CPD spectra barely depend on q and z_2 for both the shock-induced and shock-free solutions, which agrees with the findings in [19]. Also, we examine the shock parameter space in the $\lambda - E$ plane and observe how it is modified by q and z_2 . We find that as q increases, the shock parameter space shrinks, whereas it expands with an increase in z_2 . Therefore, the possibility of shock transitions is greater for smaller mass ratios and larger binary separations. Indeed, this analysis implies that while the shock properties of the CPD moderately change due to the presence of a secondary black hole, it does not significantly affect the CPD spectrum. As mentioned earlier, these results yield similar consequences of the binary mass ratio, as demonstrated in [19]. The previous study [19] analyzed the CBD accretion and its asso-

ciated spectrum in the presence of irradiation from CPD and CSD, treating all disc components as standard discs within a Newtonian framework rather than considering general relativity effects. However, in our study, we focus solely on the accretion properties of the CPD within a fully general relativistic framework. Additionally, we consider the CPD as an optically thin medium that does not emit like a black body, as is typically assumed in standard disc models. Therefore, even though our analysis differs from the work in [19], the remarks on the binary mass ratio are the same.

Finally, we mention the limitations of our work. We do not incorporate viscosity [65, 68], magnetic fields [67, 71, 72], thermal conduction [73, 74], and radiative cooling [54, 58] in the flow equations. Moreover, we only consider the thermal bremsstrahlung emission, neglecting the synchrotron and Compton emission processes [58, 75]. However, their presence in an accretion model is expected to provide more valuable insights into accretion physics. Also, we consider a binary system consisting of two Schwarzschild black holes. In reality, astrophysical black holes possess some spin. Exact analytical solutions

for a stable binary configuration of two spinning black holes are already available in the literature [76]. We expect, the spin parameters may also effect the CPD accretion flow. We plan to investigate all these aspects in future work and report our findings elsewhere.

DATA AVAILABILITY STATEMENT

The data underlying this article will be available with reasonable request.

ACKNOWLEDGMENTS

The work of SP is supported by the University Grants Commission (UGC), India, under the Senior Research Fellowship (SRF) scheme. BRM is supported by a START-UP RESEARCH GRANT from the Indian Institute of Technology Guwahati (IIT Guwahati), India, under the grant SG/PHY/P/BRM/01. SD is supported by the Science and Engineering Research Board (SERB), India, through the grant MTR/2020/000331.

-
- [1] M. C. Begelman, R. D. Blandford, and M. J. Rees, *Nature* **287**, 307 (1980).
- [2] N. Roos, *Astronomy and Astrophysics* **104**, 218 (1981).
- [3] S. Banerjee, *Monthly Notices of the Royal Astronomical Society* **467**, 524 (2017), 1611.09357.
- [4] C. L. Rodriguez, P. Amaro-Seoane, S. Chatterjee, and F. A. Rasio, *Phys. Rev. Lett.* **120**, 151101 (2018), 1712.04937.
- [5] S. DeLaurentiis, M. Epstein-Martin, and Z. Haiman, *Mon. Not. Roy. Astron. Soc.* **523**, 1126 (2023), 2212.02650.
- [6] B. P. Abbott et al. (LIGO Scientific, Virgo), *Phys. Rev. Lett.* **116**, 061102 (2016), 1602.03837.
- [7] S. Burke-Spolaor et al., *Astron. Astrophys. Rev.* **27**, 5 (2019), 1811.08826.
- [8] Z. Arzoumanian et al. (NANOGrav), *Astrophys. J. Lett.* **905**, L34 (2020), 2009.04496.
- [9] P. Amaro-Seoane, H. Audley, S. Babak, J. Baker, E. Barausse, P. Bender, E. Berti, P. Binetruy, M. Born, D. Borraioni, et al., arXiv preprint arXiv:1702.00786 (2017).
- [10] A. Mangiagli, C. Caprini, M. Volonteri, S. Marsat, S. Vergani, N. Tamanini, and H. Inchauspé, *Phys. Rev. D* **106**, 103017 (2022), 2207.10678.
- [11] C. Roedig, J. H. Krolik, and M. C. Miller, *Astrophys. J.* **785**, 115 (2014), 1402.7098.
- [12] D. J. D’Orazio, Z. Haiman, P. Duffell, B. D. Farris, and A. I. MacFadyen, *Monthly Notices of the Royal Astronomical Society* **452**, 2540 (2015), 1502.03112.
- [13] M. J. Graham, S. G. Djorgovski, D. Stern, A. J. Drake, A. A. Mahabal, C. Donalek, E. Glikman, S. Larsen, and E. Christensen, *Mon. Not. Roy. Astron. Soc.* **453**, 1562 (2015), 1507.07603.
- [14] M. J. Graham, S. G. Djorgovski, D. Stern, E. Glikman, A. J. Drake, A. A. Mahabal, C. Donalek, S. Larson, and E. Christensen, *Nature* **518**, 74 (2015), 1501.01375.
- [15] T. Liu, S. Gezari, M. Ayers, W. Burgett, K. Chambers, K. Hodapp, M. E. Huber, R. P. Kudritzki, N. Metcalfe, J. Tonry, et al., *Astrophys. J.* **884**, 36 (2019), 1906.08315.
- [16] M. L. Saade, D. Stern, M. Brightman, Z. Haiman, S. G. Djorgovski, D. D’Orazio, K. E. S. Ford, M. J. Graham, H. D. Jun, R. P. Kraft, et al., *Astrophys. J.* **900**, 148 (2020), 2001.08870.
- [17] T. Bogdanovic, M. C. Miller, and L. Blecha, *Living Rev. Rel.* **25**, 3 (2022), 2109.03262.
- [18] E. M. Gutiérrez, L. Combi, S. C. Noble, M. Campanelli, J. H. Krolik, F. López Armengol, and F. García, *Astrophys. J.* **928**, 137 (2022), 2112.09773.
- [19] Y. Lee, A. T. Okazaki, and K. Hayasaki, *Astrophys. J.* **975**, 141 (2024), 2407.13366.
- [20] S. Mondal, M. Das, K. Rubinur, K. Bansal, A. Nath, and G. B. Taylor, *Astron. Astrophys.* **691**, A279 (2024), 2409.05717.
- [21] E. M. Gutiérrez, L. Combi, and G. Ryan (2024), 2405.14843.
- [22] A. Sesana, A. Gualandris, and M. Dotti, *Monthly Notices of the Royal Astronomical Society* **415**, L35 (2011), 1105.0670.
- [23] D. B. Bowen, V. Mewes, S. C. Noble, M. Avara, M. Campanelli, and J. H. Krolik, *Astrophys. J.* **879**, 76 (2019), 1904.12048.
- [24] F. G. Lopez Armengol, L. Combi, M. Campanelli, S. C. Noble, J. H. Krolik, D. B. Bowen, M. J. Avara, V. Mewes, and H. Nakano, *Astrophys. J.* **913**, 16 (2021), 2102.00243.

- [25] L. Combi, F. G. Lopez Armengol, M. Campanelli, S. C. Noble, M. Avara, J. H. Krolik, and D. Bowen, *Astrophys. J.* **928**, 187 (2022), 2109.01307.
- [26] E. M. Gutiérrez, L. Combi, G. E. Romero, and M. Campanelli, *Mon. Not. Roy. Astron. Soc.* **532**, 506 (2024), 2301.04280.
- [27] E. Liang and K. Thompson, *The Astrophysical Journal* **240**, 271 (1980).
- [28] M. A. Abramowicz and W. Zurek, *The Astrophysical Journal* **246**, 314 (1981).
- [29] M. Astorino and A. Viganò, *Phys. Lett. B* **820**, 136506 (2021), 2104.07686.
- [30] D. Kramer and G. Neugebauer, *Physics Letters A* **75**, 259 (1980).
- [31] W. Dietz and C. Hoenselaers, *Annals of Physics* **165**, 319 (1985).
- [32] S. D. Majumdar, *Phys. Rev.* **72**, 390 (1947).
- [33] A. Papapetrou, in *Proceedings of the Royal Irish Academy. Section A: Mathematical and Physical Sciences* (JSTOR, 1945), vol. 51, pp. 191–204.
- [34] J. B. Hartle and S. W. Hawking, *Commun. Math. Phys.* **26**, 87 (1972).
- [35] R. Emparan, *Physical Review D* **61**, 104009 (2000).
- [36] G. M. de Castro and P. S. Letelier, *Classical and Quantum Gravity* **28**, 225020 (2011).
- [37] R. Bach and H. Wevl, *Mathematische Zeitschrift* **13**, 134 (1922).
- [38] W. Israel and K. Khan, *Il Nuovo Cimento* (1955-1965) **33**, 331 (1964).
- [39] M. S. Costa and M. J. Perry, *Nuclear Physics B* **591**, 469 (2000).
- [40] G. A. Alekseev and V. A. Belinski, *Gen. Rel. Grav.* **51**, 68 (2019), 1905.05317.
- [41] L. Rezzolla and O. Zanotti, *Relativistic Hydrodynamics* (Oxford University Press, 2013), ISBN 978-0-19-174650-5, 978-0-19-852890-6.
- [42] I. K. Dihingia, S. Das, D. Maity, and S. Chakrabarti, *Physical Review D* **98**, 083004 (2018).
- [43] J. Lu, *Astronomy and Astrophysics* **148**, 176 (1985).
- [44] J. Peitz and S. Appl, *Mon. Not. Roy. Astron. Soc.* **286**, 681 (1997), astro-ph/9612205.
- [45] R. Yarza, G. N. Wong, B. R. Ryan, and C. F. Gammie, *Astrophys. J.* **898**, 50 (2020), 2006.01145.
- [46] F. Yuan and R. Narayan, *Ann. Rev. Astron. Astrophys.* **52**, 529 (2014), 1401.0586.
- [47] J. Lasota, in *Theory of Accretion Disks—2: Proceedings of the NATO Advanced Research Workshop on Theory of Accretion Disks—2 Garching, Germany March 22–26, 1993* (Springer, 1994), pp. 341–349.
- [48] H. Riffert and H. Herold, *Astrophysical Journal* v. 450, p. 508 **450**, 508 (1995).
- [49] I. Chattopadhyay and D. Ryu, *The Astrophysical Journal* **694**, 492 (2009).
- [50] I. Chattopadhyay and R. Kumar, *Mon. Not. Roy. Astron. Soc.* **459**, 3792 (2016), 1605.00752.
- [51] R. Kumar and I. Chattopadhyay, *Monthly Notices of the Royal Astronomical Society* **469**, 4221 (2017).
- [52] S. Patra, B. R. Majhi, and S. Das, *JCAP* **01**, 060 (2024), 2308.12839.
- [53] I. D. Novikov and K. S. Thorne, *Black holes (Les astres occlus)* **1**, 343 (1973).
- [54] S. Sarkar and I. Chattopadhyay, *Int. J. Mod. Phys. D* **28**, 1950037 (2018), 1811.05947.
- [55] I. K. Dihingia, S. Das, and S. Mandal, *Journal of Astrophysics and Astronomy* **39**, 1 (2018).
- [56] I. K. Dihingia, S. Das, G. Prabhakar, and S. Mandal, *Monthly Notices of the Royal Astronomical Society* **496**, 3043 (2020).
- [57] S. Sarkar, I. Chattopadhyay, and P. Laurent, *Astronomy & Astrophysics* **642**, A209 (2020).
- [58] S. Sarkar and I. Chattopadhyay, *Journal of Astrophysics and Astronomy* **43**, 34 (2022).
- [59] I. K. Dihingia, D. Maity, S. Chakrabarti, and S. Das, *Physical Review D* **102**, 023012 (2020).
- [60] G. Sen, D. Maity, and S. Das, *JCAP* **08**, 048 (2022), 2204.02110.
- [61] J.-P. Luminet, *Astronomy and Astrophysics* **75**, 228 (1979).
- [62] D. Maoz, *Astrophysics in a Nutshell*, vol. 16 (Princeton university press, 2016).
- [63] S. L. Shapiro and S. A. Teukolsky, *Black holes, white dwarfs, and neutron stars: The physics of compact objects* (John Wiley & Sons, 2008).
- [64] G. B. Rybicki and A. P. Lightman, *Radiative processes in astrophysics* (John Wiley & Sons, 1991).
- [65] I. Dihingia, S. Das, D. Maity, and A. Nandi, *Mon. Not. Roy. Astron. Soc.* **488**, 2412 (2019), 1903.02856.
- [66] S. Patra, B. R. Majhi, and S. Das, *Phys. Dark Univ.* **37**, 101120 (2022), 2202.10863.
- [67] S. Mitra and S. Das, *Astrophys. J.* **971**, 28 (2024), 2405.16326.
- [68] S. Patra, B. R. Majhi, and S. Das, *JHEAp* **44**, 371 (2024), 2407.07968.
- [69] P. A. Becker and D. Kazanas, *Astrophys. J.* **546**, 429 (2001), astro-ph/0101020.
- [70] A. H. Taub, *Phys. Rev.* **74**, 328 (1948).
- [71] S. Mitra, D. Maity, I. K. Dihingia, and S. Das, *Mon. Not. Roy. Astron. Soc.* **516**, 5092 (2022), 2204.01412.
- [72] I. K. Dihingia and Y. Mizuno, *Astrophys. J.* **967**, 4 (2024), 2403.18359.
- [73] S. Mitra, S. M. Ghoreyshi, A. Mosallanezhad, S. Abbassi, and S. Das, *Mon. Not. Roy. Astron. Soc.* **523**, 4431 (2023), 2306.02453.
- [74] M. Singh and S. Das (2024), 2408.02256.
- [75] I. K. Dihingia, S. Das, G. Prabhakar, and S. Mandal, *Mon. Not. Roy. Astron. Soc.* **496**, 3043 (2020), 1911.02757.
- [76] M. Astorino and A. Viganò, *Eur. Phys. J. C* **82**, 829 (2022), 2105.02894.